Biomedical Mathematics: Promising Directions
in Imaging, Therapy Planning, and Inverse Problems
Y. Censor, M. Jiang, G. Wang, Editors

Statistical Iterative Reconstruction for X-Ray Computed Tomography

Bruno De Man[1*] and Jeffrey A. Fessler[2]
[1]GE Global Research, Niskayuna, New York
deman@ge.com
[2]Electrical Engineering and Computer Science Department
University of Michigan, Ann Arbor, Michigan
fessler@eecs.umich.edu

1 Introduction

The first *X-ray computed tomography* (CT) prototypes by Cormack[1,2], Ambrose[3], and Hounsfield[4] acquired a limited set of X-ray pencil beam measurements. This resulted in a number of linear equations (line integrals) and a comparable number of unknowns (attenuation coefficients). These equations were solved algebraically with the so-called *algebraic reconstruction technique* (*ART*).[5.6] The basic ART scheme is an iterative reconstruction (IR) algorithm solving one measurement at a time by updating all corresponding (image) pixels or voxels:

$$\mu_j^{n+1} = \mu_j^n + I_{ij} \frac{p_i - \sum_k I_{ij} \mu_k^n}{\sum_k I_{ik}^2} \quad \text{for} \quad i = n \bmod I + 1. \tag{1}$$

All symbols used in this paper are summarized in the following table:

$\mu_i^n, \mu(x,y)$	linear attenuation coefficient	$\tilde{p}_i, \tilde{p}_m(s)$	filtered projection data
N,N	iteration number, total number of iterations	$h(s)$	ramp filter kernel
j,J	voxel index, total number of voxels	θ_m	view angle of view number m
I_{ij}	interpolation coefficient or element of the system matrix	$\otimes$	convolution

*Corresponding author.

$p_i, p_m(s)$	attenuation line integral measurement or projection data	y_i	intensity measurement
i, I	line integral index, total number of line integrals	e_i	intensity measurement noise
x, y	voxel coordinates	$\overline{y}_i$	intensity expected value
m, M	view number, total number of views	s, S	sample index, total number of samples

The introduction of filtered backprojection (FBP) by Shepp[7] in 1974 started a new class of much faster CT reconstruction algorithms. This technique was inherited from other applications in astronomy[8] and electron microscopy[9]. The simplest two-dimensional (2D) parallel-beam FBP formula is given by:

$$\mu(x,y) = \sum_{m=1}^{M} \tilde{p}_m \left(x\cos\theta_m + y\sin\theta_m \right) \quad \text{where} \quad \tilde{p}_m(s) = p_m(s) \otimes h(s), \tag{2}$$

where usually one must apodize the ramp filter $h(s)$ to control noise and aliasing artifacts. The application of FBP to x-ray CT has seen enormous advances and fine-tuning for many years, and until today it remains the reconstruction method used in all commercial CT systems. Ironically, after having gone from iterative reconstruction techniques like ART to direct reconstruction techniques like FBP, there recently is a lot of renewed interest in applying iterative reconstruction (IR) to CT. Functional imaging modalities (PET and SPECT) have already adopted *statistical iterative reconstruction* (*SIR*) for many years[10,11,12], driven by the IQ needs of these essentially quantum noise limited modalities. In CT, the high computational cost of IR and the high requirements for throughput and time-to-first-image are the reasons that IR has not yet been adopted commercially. Some of the first applications of SIR to real CT data started in the late 1990s[13–18], and were inspired by its capability to model the physics of the CT acquisition and its robustness to missing data. More recently, research groups started applying iterative reconstruction methods to clinical data, leading to promising clinical results.[19–21]

2 Bayesian Framework

The starting point for most SIR algorithms is a cost function based on statistical models:

$$\text{reconstructed image} = \arg\max_{\text{image}} P\left(\text{image} \middle| \text{measurements} \right)^{e} \tag{3}$$

This represents a quest for the most likely image, given the measurements. Applying Bayes rule, using the monotonicity of the logarithm and dropping the constant term, this formulation is equivalent to the following optimization problem:

$$\text{reconstructed image} = \arg\max_{\text{image}} \left[P\left(\text{measurements} \middle| \bar{y}\left(\text{image}\right)\right) + P\left(\text{image}\right) \right] \tag{4}$$

The first term is called the likelihood term and describes the probability of the measurements given the image, or more specifically given the model $\bar{y}$ (*image*) for the measurement means. The second term is the prior term. With prior information, this optimization problem is called the *maximum a posteriori* (*MAP*) approach. Without prior information, the second term drops out and it becomes the *maximum likelihood* (*ML*) approach. We will now describe how to calculate the components of this cost function one by one.

3 Forward Models and Projectors

The core of an SIR algorithm is its forward model $\bar{y}$ (*image*) and more specifically the projector-backprojector. X-ray CT measurements are governed by Beer's law:

$$\bar{y}_i = A_i \exp\left(-p_i\right) \tag{5}$$

where the overbar refers to the calculated (or expected) value, as opposed to the actual measurements and A_i is the expected air scan measurement. The argument of the exponent is computed by a Radon transform or projection:

$$p_i = \sum_{j=1}^{J} I_{ij} \mu_j \tag{6}$$

where the coefficients I_{ij} represent (or approximate) the intersection length between projection line i and voxel j. We now present a few popular approaches for computing I_{ij} and performing the projection operation. The key is to find the best tradeoff between accuracy and computational efficiency.

3.1 Intersection Length

This method described in Herman[22], Siddon[23], and Zeng[24] is perhaps the most intuitive approach to approximating the line integrals: each coefficient I_{ij} is computed as the intersection

length between line i and voxel j, either in 2D or in 3D. This is shown schematically in Figure 1(a), where the contribution of voxels 1 and 2 to projection line i is computed as:

$$p_i += L_1\mu_1 + L_2\mu_2. \quad [7]$$

3.2 Linear Interpolation (Joseph's Method)

Another intuitive approach was described in Joseph[25]: the coefficients are computed in 2D as the row intersection length combined with the linear interpolation between the two nearest voxels within that row, and in 3D as the slab intersection length combined with bi-linear interpolation between the four nearest voxels within that slab. This is shown schematically in Figure 1(b), where the contribution of voxels 1 and 2 to projection line i is computed as:

$$p_i += L\frac{a_2\mu_1 + a_1\mu_2}{a_1 + a_2}. \quad (8)$$

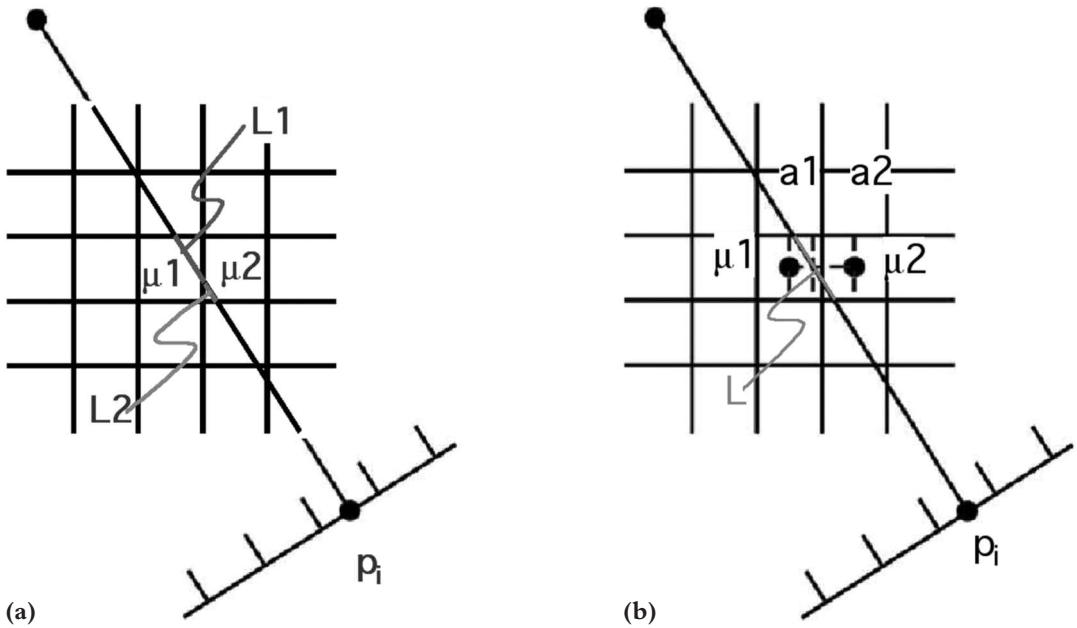

Figure 1. Schematic representation of (a) the line intersection method and (b) Joseph's linear interpolation method. SEE COLOR PLATE XX.

3.3 Linear Interpolation with General Step-Size

In this more general method the projection line is divided into a number of segments with fixed step size.[26] At each step, the contribution to projection line i is computed as the product of the step-size and a voxel value obtained by bi-linear interpolation between the four nearest voxels (in 2D) or obtained by tri-linear interpolation between the eight nearest voxels (in 3D). For 2D, this is shown schematically in Figure 2(a), where the contribution for a given line segment with length ε is computed as:

$$p_i += \varepsilon \frac{a_2 b_2 \mu_1 + a_1 b_2 \mu_2 + a_2 b_1 \mu_3 + a_1 b_1 \mu_4}{\left(a_1 + a_2\right)\left(b_1 + b_2\right)}. \tag{9}$$

If the step-size ε is chosen to be equal to the step-size between two consecutive rows or slabs, this method reduces to Joseph's method.

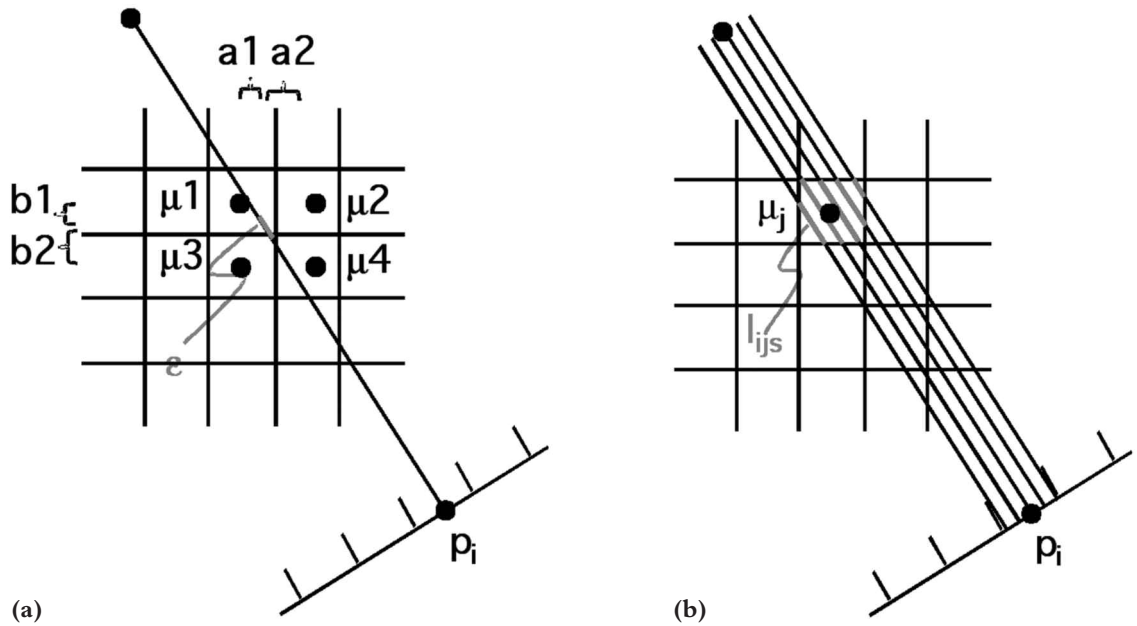

Figure 2. Schematic representation of (a) the linear interpolation method with general step size and (b) the solid voxel or strip integral method. SEE COLOR PLATE XX.

3.4 Distance-Driven Method

The recently proposed "distance-driven" projector-backprojector method[27,28] was motivated by the following desired properties:

- low arithmetic cost
- sequential memory access
- good approximation to the true strip integral
- continuous signals should be (back-)projected onto continuous signals.

In this method, the coefficients are computed as the *row* or *slab* intersection length combined with the *overlap coefficient*. The overlap coefficient is computed based on the length or area of overlap between a voxel and a detector cell when they are mapped onto each other as seen by the source. This is shown schematically in Figure 3(a) in 2D, where the contribution of two voxels to projection line i is computed as:

$$p_i \mathrel{+}= L_1 \frac{o_1 \mu_1 + o_2 \mu_2}{o_1 + o_2}. \tag{10}$$

Efficient implementation can be achieved by mapping the detector cell boundaries on the x- or y-axis, computing the projection or backprojection for one row at the time, and looping across all voxel and detector cell boundaries from left to right. Figure 3(b,c) show the corrsponding

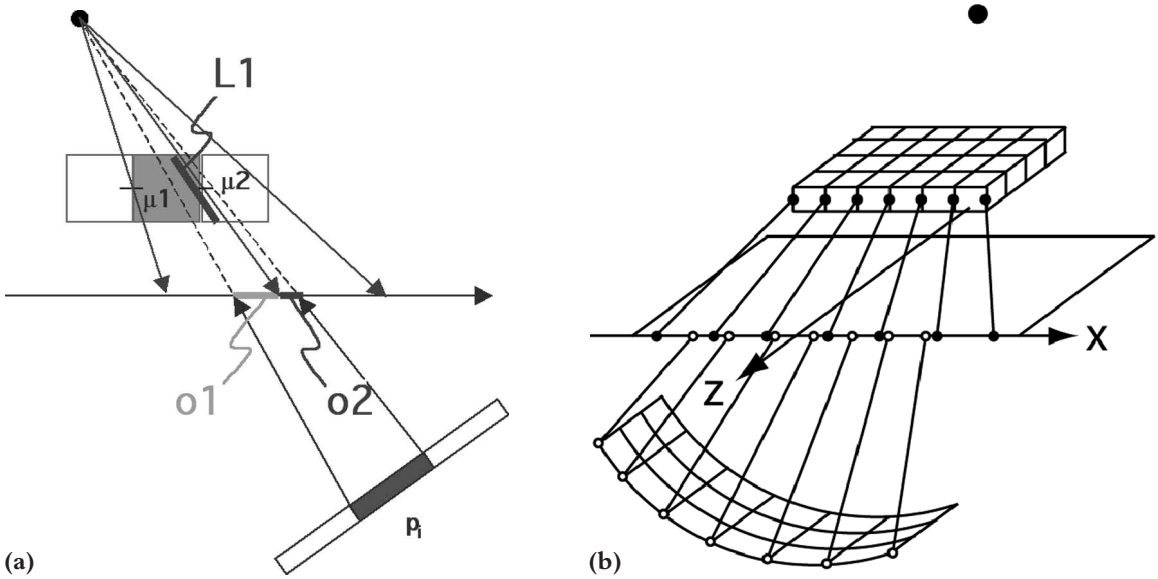

Figure 3. Schematic representation of (a) the 2D distance-driven method and (b,c) the 3D distance-driven method. SEE COLOR PLATE XX.

3D overlap segments. The overlap area is computed as the product of the overlap lengths in x-y and and in z, respectively.

3.5 Methods Based on Basis Functions

The methods summarized above can be described as procedures for forward projection, but they are not all based on explicit models. Another family of methods is based on basis function expansions of the linear attenuation coefficient distribution[29–32] of the form:

$$\mu(\vec{r}) = \sum_j \mu_j b_j(\vec{r}), \tag{11}$$

where $\vec{r}$ denotes 2D or 3D continuous-space coordinates. Numerous choices for basis functions have been considered explicitly or implicitly in the literature. There are several factors that influence the choice of basis functions. Mathematically, we require linear independence of the basis functions to ensure uniqueness of the expansion. The stronger condition of orthogonality may be desirable in some cases but usually is not essential. We would like to approximate $\mu(\vec{r})$ well for a given number of terms, including representing a uniform (constant) object well. Computationally, we prefer bases for which the I_{ij} values are sparse. Nonnegative bases are preferable when we want to enforce non-negativity of . Basis functions that have been investigated include the following: square voxels[20], Fourier series[33], circular harmonics[1,2,34,35], wavelets[36], overlapping circles (disks)[11,37,38] or spheres (balls)[39], Kaiser-Bessel window functions (blobs)[40], "natural pixels"[41–45], B-splines[31,46,47], Dirac impulses, Gaussian functions[48–50], organ-based basis functions[51–56], and others.[57] Other related representations include polygons[58], polar grids[59–61], logarithmic polar grids[62], and tetrahedral meshes[63]. For computation, rotationally symmetric basis functions can be convenient. Kaiser-Bessel functions (blobs) have been a particularly popular choice of rotationally symmetric basis. Although in the context of SPECT imaging, blobs were not found to be advantageous[64], more favorable results have been reported in X-ray and PET.[21,65–70] Naturally, the fineness of the grid can affect edge artifacts and aliasing.[15,71]

3.6 Finite Beam Width

Consider a monoenergetic x-ray source for simplicity of presentation. Ideally the i^{th} measurement would be associated with a line integral from an ideal point source to an ideal point detector. A more realistic forward model is achieved by summing a number of projection line to approximate the finite x-ray beam.[20,72,73] The result is a good approximation of the true strip or x-ray beam integral. This is shown schematically in Figure 2(b), where the contribution of voxel j to projection line i is computed as:

$$p_i += \frac{1}{S} \sum_{s=1}^{S} I_{ijs} \mu_j. \tag{12}$$

It was shown in De Man[73] that the artifacts due to the nonlinear nature of the partial volume effect[73,74] can be prevented by performing the summation over the samples s outside of the exponent:

$$p_i = \log\left(\frac{1}{S} \sum_{s=1}^{S} \exp\left(-\sum_{j=1}^{J} I_{ijs} \mu_j \right) \right). \tag{13}$$

Computing the system matrix elements is simplified if the basis functions are rotationally symmetric, because then the footprint is independent of (parallel-beam) projection angle. The Kaiser-Bessel basis, also known as blobs, is the most popular of the rotationally symmetric basis functions, because they are approximately band limited, and by carefully adjusting the parameters they approximate a partition of unity.[67,68]

3.7 Fourier-based Projection Methods

A drawback of the preceding methods is that they require $O(N^3)$ operations for $N \times N$ images and N projection views. By using the Fourier-slice theorem for the Radon transform, one can develop an $O(N^2 \log N)$ reprojection approach for 2D parallel beam and fan-beam geometries.[76–78] The method first takes the 2D fast Fourier transform (FFT) of the image, then interpolates the Fourier samples onto a polar grid. An inverse FFT, followed by parallel-to-fan rebinning, completes the projection operation. Open-source software for this method is available.[79] It is straightforward conceptually to generalize this approach to 3D parallel-beam geometries such as those used in fully 3D PET.[76] Unfortunately, it is unclear how to generalize this method to 3D cone-beam CT (axial or helical) geometries efficiently. Other $O(N^2 \log N)$ methods have been proposed based on hierarchical decompositions.[80,81]

4 Noise Models

A second aspect of SIR is the noise model. Realizing that the actual measurements include noise and deviate from their expected value, we can write:

$$y_i = \bar{y}_i + e_i. \tag{14}$$

While energy-integrating detectors are better approximated by a *compound Poisson* quantum noise model combined with a *Gaussian* electronic noise model, most researchers approximate the total noise by a Poisson model:

$$P\left(y_i \middle| \bar{y}_i\right) = \frac{e^{-\bar{y}_i} \bar{y}_i^{y_i}}{y_i!} \tag{15}$$

or by a Gaussian model:

$$P\left(y_i \middle| \bar{y}_i\right) = \frac{1}{\sigma_y \sqrt{2\pi}} \exp\left(-\frac{\left(y_i - \bar{y}_i\right)^2}{2\sigma_y^2} \right). \tag{16}$$

The incremental benefit of a more accurate noise model has been studied[81] but has not been demonstrated to be advantageous in typical imaging scenarios. All the above noise models implicitly take into account that the noise variance is proportional to the mean signal, which is one of the main strengths of SIR. Relatively more weight will be given to reliable measurements, and less weight will be given to noisy measurements. This leads to reduced noise in the reconstructed image for a given patient dose and spatial resolution.

5 Priors and Regularizers

The prior or regularization term defines a criterion for voxels to deviate minimally from their neighbors or from predefined values. The most popular are *Gibbs neighborhood priors*, which are generally defined by the following probability:

$$P\left(\left\{\mu_j\right\}\right) \sim \prod_{j=1}^{J} \prod_{k=1}^{J} \exp\left(-N_{jk} \phi\left(\mu_j - \mu_k\right)\right), \tag{17}$$

where the neighborhood mask N_{jk} is typically defined by:

$$N_{jk} = \frac{1}{\sqrt{\left(x_j - x_k\right)^2 + \left(y_j - y_k\right)^2}} \quad \text{when j and k are neighbor 0 elsewhere.}$$

For a *quadratic* prior[83], the potential function ϕ is a quadratic function, leading to the following probability:

$$P\left(\left\{\mu_j\right\}\right) \sim \prod_{j=1}^{J} \prod_{k=1}^{J} \frac{1}{\sigma_\mu \sqrt{2\pi}} \exp\left(-N_{jk} \frac{\left(\mu_j - \mu_k\right)^2}{2\sigma_\mu^2} \right). \tag{18}$$

An edge-preserving behavior can be obtained by using a *Huber* prior[84], which has a potential function that becomes linear for larger arguments:

$$\phi\left(\mu\right) = \begin{array}{ll} \dfrac{\mu^2}{2} & \text{for } \left|\mu\right| \le \delta \\ \delta\left(\left|\mu\right| - \delta/2\right) & \text{for } \left|\mu\right| > \delta \end{array} \tag{19}$$

or a *Geman* prior[85], which has a potential function that becomes constant for larger arguments:

$$\phi\left(\mu\right) = \frac{\mu^2 \sigma_\mu^2}{\mu^2 + \sigma_\mu^2}. \tag{20}$$

The latter has the disadvantage of being non-convex, which leads to local minima in the cost function, potentially causing convergence problems.

The *generalized Gaussian* prior[86] is similar to the quadratic prior but with a different exponent, also providing more edge-preserving behavior:

$$\phi(\mu) = \mu^n. \tag{21}$$

We proposed a Generalized Geman prior[87] that offers the ability to fine tune the prior characteristics:

$$\phi\left(\mu\right) = \frac{\mu^2 \sigma_\mu^n}{2\left(\sqrt{\mu^2/2 + \sigma_\mu^2/2}\right)^2}. \tag{22}$$

Figure 4 illustrates its properties for various values of n. We proved that it is convex for $n < 16/17$.

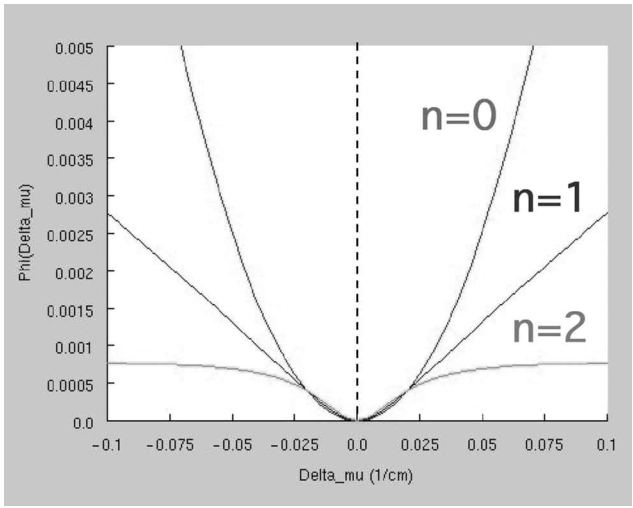

Figure 4. Generalized Geman prior for different exponents *n,* resulting in a quadratic prior ($n=0$), a Huber-like prior ($n=1$) and a Geman prior ($n=2$). SEE COLOR PLATE XX.

6 Update Steps

In a model-based image reconstruction method, all of the above elements (system model, statistical model, and regularizer) are combined into a single cost function. An optimization algorithm is applied to the cost function to produce the reconstructed image. A SIR method is the combination of the cost function and the selected optimizer or update step or iterative algorithm. Numerous iterative algorithms have been investigated for image reconstruction, including both general purpose methods and methods tailored to the form of the specific cost functions of interest in tomography. The challenge is to find a technique that converges in few iterations and has a low computation cost per iteration.

Several factors affect the choice of iterative algorithm, including the form of the cost function, whether non-negativity constraints are to be enforced, and what type of parallelization is desired. The implementation of the system matrix can also affect the algorithm choice. For example, the Fourier-based system methods described above are efficient only if all (or nearly all) the projection views are computed together, which is poorly matched to ordered-subsets algorithms that work with a small subset of the projection views at a time. Other hierarchical decomposition methods for forward- and backprojection share this limitation. System models based on "factored system matrices," e.g., Mumcuoglu[84,88], Qi[89], Reader[90], are convenient for gradient-based algorithms that update all voxels simultaneously, but are poorly suited to algorithms that access individual rows or columns of the system matrix at a time.

Hereafter we focus on algorithms for the penalized weighted least-squares (PWLS) cost functions of the form

$$\Psi(\mu) = \sum_i w_i \left(p_i - \sum_j I_{ij} \mu_j \right)^2 + R(\mu). \tag{23}$$

where the regularizer $R(\mu)$ is the negative logarithm of one of the priors described above, and the weights w_i of the Gaussian noise model are the reciprocal of an estimate of the variance of the log projection data p_i. Often $w_i = y_i$ is used, which corresponds to a noise model where the variance equals the mean. For a review of algorithms for the Poisson model, see Fessler.[91] Algorithms based on the quadratic data-fit term in equation (23) are appropriate for monoenergetic transmission measurements, but may be suboptimal for polyenergetic measurements with energy-integrating detectors. For polyenergetic data there is a nonlinear relationship between the measured and the true attenuation lengths, requiring a more complicated forward model and data-fit term.[16,17,92,93]

6.1 Gradient-based Updates Steps

For minimizing the above cost function, the conjugate gradient (CG) method and other gradient-based update steps optimize all voxels simultaneously, and therefore are particularly convenient for parallelization. An example of a weighted least-squares (WLS) update step[94] is given by:

$$\mu_j^{n+1} = \mu_j^n + \frac{\sum_i I_{ij} w_i \left(p_i - \sum_{k=1,S} I_{ik} \mu_k^n \right)}{\sum_i I_{ik} w_i \sum_{\xi=1,S} I_{i\xi}}. \tag{24}$$

The resulting flow of operations is represented schematically in Figure 5: the current image estimate is projected, the resulting computed sinogram is compared to the measured sinogram, the error term is backprojected, and the result is added to the image estimate. However, such gradient-based methods often require a large number of iterations to converge. For quadratic regularization methods, there are simple analytical expressions for the step-size that minimizes the cost function along a given search direction. In contrast, nonquadratic (e.g., edge preserving) regularizers require line search methods for each search direction. A line search approach that ensures monotonic descent by using optimization transfer principles[95] is described in Fessler.[96]

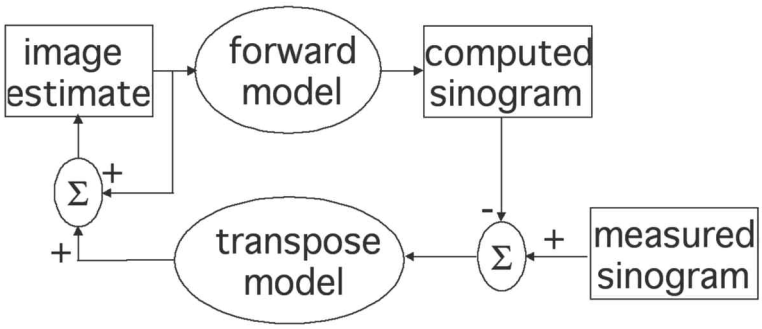

Figure 5. Iterative reconstruction scheme consisting of a forward model and a negative feedback of the error sinogram via the transpose of the forward model.

6.2 Single Coordinate Update Steps

Iterative coordinate descent (ICD) methods optimize one voxel at a time, holding all other voxels fixed, and cycle through the voxels one by on in some order.[20,97–100] The WLS ICD update step is given by:

$$\delta_j^{n+1} = \frac{\sum_i w_i \left(p_i - \bar{p}_i^n \right) I_{ij}}{\sum_i w_i I_{ij}^2}. \tag{25}$$

This method converges rapidly in tomographic image reconstruction problems. Non-uniform updating schemes can accelerate convergence.[101]

6.3 Ordered-Subsets Acceleration

For fully 3D iterative reconstruction in PET, modern commercial scanners use (unregularized) order subsets (OS) methods that compute updates based on alternating subsets of measured projection views.[12,102] Standard OS algorithms "converge" much faster in the early iterations, but they typically approach a limit cycle rather than converging to a minimizer of the cost function. Convergence can be restored by modifying the algorithm with relaxation parameters[103] or with modified surrogate functions.[104] However, these modifications may also slow down the convergence rate somewhat.

6.4 Hybrid Approaches

In between ICD and gradient-based updates are grouped-coordinate descent algorithms that use all the data to update a subset of the pixels each (sub)iteration.[100,105,106] These algorithms offer a compromise that combines efficient iterations with faster convergence than gradient-based methods, albeit with somewhat more complicated implementation.

6.5 Algebraic Reconstruction Techniques

In contrast to algorithms that are designed to minimize a cost function based on the data statistics, the algebraic reconstruction technique (ART) and its relatives are based on projection methods for solving the system of equations $p = A\mu$, where p denotes the data, A denotes the system model, and μ denotes the unknown voxel values. One variant of the ART algorithm is the simultaneous ART (SART) algorithm that has the form:

$$\mu^{n+1} = \mu^n + \omega D_1 A' D_2 \left(p - A\mu^n \right), \tag{26}$$

where D_1 denotes a diagonal matrix with elements $1 \Big/ \sum_i I_{ij}$ along its diagonal, and D_2 denotes a diagonal matrix with elements $1 \Big/ \sum_i I_{ij}$ along its diagonal. The relaxation parameter ω must lie within a certain interval to ensure convergence.[107] If it converges, it finds a minimizer of a WLS cost function with weights $1 \Big/ \sum_i I_{ij}$. These weights are unrelated to the data statistics, so one cannot expect the standard SART algorithm to perform well for very noisy data. However, if we modify the original system of equations $p = A\mu$ by multiplying by a suitable diagonal matrix to form the system $\tilde{p} = \tilde{A}\mu$, where $\tilde{p}_i = p_i w_i \sum_j I_{ij}$ and $\bar{I}_{ij} = I_{ij} w_i \sum_j I_{ij}$, then the corresponding SART algorithm for the modified system of equations is

$$\mu^{n+1} = \mu^n + \omega D_3 A' W \left(p - A\mu^n \right), \tag{27}$$

where W is diagonal with elements w_i, and D_3 is diagonal with elements $1 \Big/ \sum_i w_i I_{ij} a_i$ where $a_i = \sum_j I_{ij}$. Using optimization transfer methods, one can show that this iteration monotonically decreases the WLS cost function every iteration for $\omega = 1$. This is still for an unregularized cost function however, and it is not clear how to extend ART and its relatives to nonquadratic (edge

preserving) potential functions. In contrast, algorithms that are designed for cost functions (rather than systems of equations), such as CG, ICD, and optimization transfer methods, can readily accommodate a wide variety of regularizers.

6.6 Convergence

Ideally, only the cost function will determine the final image quality. If the cost function has a unique optimum (e.g., is convex), and one uses a sufficient number of iterations of a convergent algorithm, then the resulting image will be independent of the optimizer. The optimizer will only affect compute time. On the other hand, if the algorithm is not globally convergent or if insufficient iterations are used, then the resulting image will depend on the optimizer. Figure 6 shows a comparison[100] of different approaches as a function of iteration number. This also illustrates that some approaches—like OS—require many iterations[1] to converge, but each iteration is relatively computationally efficient. Other approaches—like ICD—converge in few iterations, but each

[1] One iteration is defined as one update of every voxel in the reconstructed image.

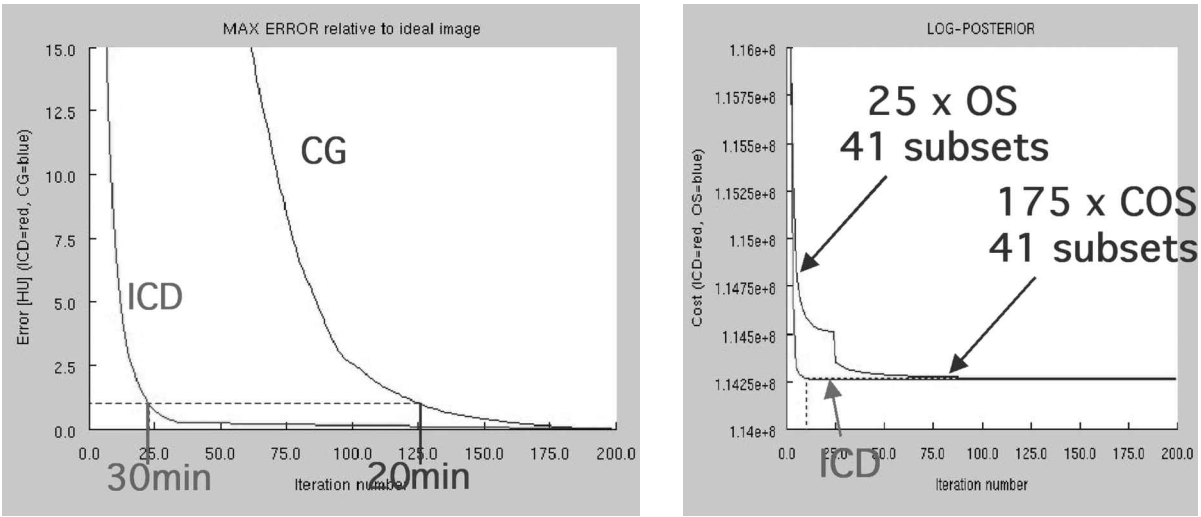

(a) **(b)**

Figure 6. (a) Image error relative to the absolute minimum as a function of iteration number for ICD and CG. (b) Cost function value as a function of iteration number for ICD and OS, switching to convergent OS after 25 iterations. SEE COLOR PLATE XX.

iteration requires a lot of computation time. Compute time per iteration depends greatly on the computing hardware, and there are currently many investigations into using graphical processing units (GPUs) and other computing devices to accelerate computation.

7 Image Quality

Images that are reconstructed by model-based image reconstruction methods have spatial resolution properties that depend on the system model, the noise statistics, and the regularizer. These terms can have somewhat unexpected interactions. In particular, when using the non-uniform weighting associated with Poisson or Poisson-like statistical model, the resulting spatial resolution can be highly non-uniform if one uses conventional regularizers.[108]

If desired, one can overcome this non-uniformity by designing modified regularizers that use values for the neighborhood weights N_{jk} that depend on the data statistics and system model. Several such design methods have been proposed for a variety of system geometries including 2D parallel-beam[108–110], 2D fan-beam[111], 3D parallel-beam[112], and 3D axial cone-beam CT.[113] The case of helical cone-beam CT remains a challenging open problem. These methods have been best characterized in the context of quadratic regularization methods, although recently there has been progress on understanding the resolution properties of nonquadratic regularization as well.[114]

Another approach for mitigating the undesired impact of the noise statistics on the local spatial resolution is to artificially adjust the weight of the respective measurements. Instead of defining the weights purely based on the noise variance of the corresponding measurements, the weights can be relaxed to avoid highly non-uniform and non-isotropic spatial resolution.[115]

Not only does SIR typically result in a much improved noise-resolution tradeoff, but the noise has a different texture, the spatial resolution is strongly object and statistics dependent, and dedicated IQ metrics are desired for SIR. We have developed a way to quantify spatial resolution and image noise as a function of location and object contrast.[116] Starting from any sinogram, such as from a real measurement, we add artificial noise and we add the projections of small wires that act as impulse responses. We reconstruct three different sinograms with the same algorithm: the original sinogram, the original-plus-noise sinogram, and the original-plus-noise-plus-impulses sinogram. We subtract the resulting images to obtain a noise-only image based on which the noise is assessed, and an impulse-only image based on which the spatial resolution is assessed. This is shown schematically in Figure 7.

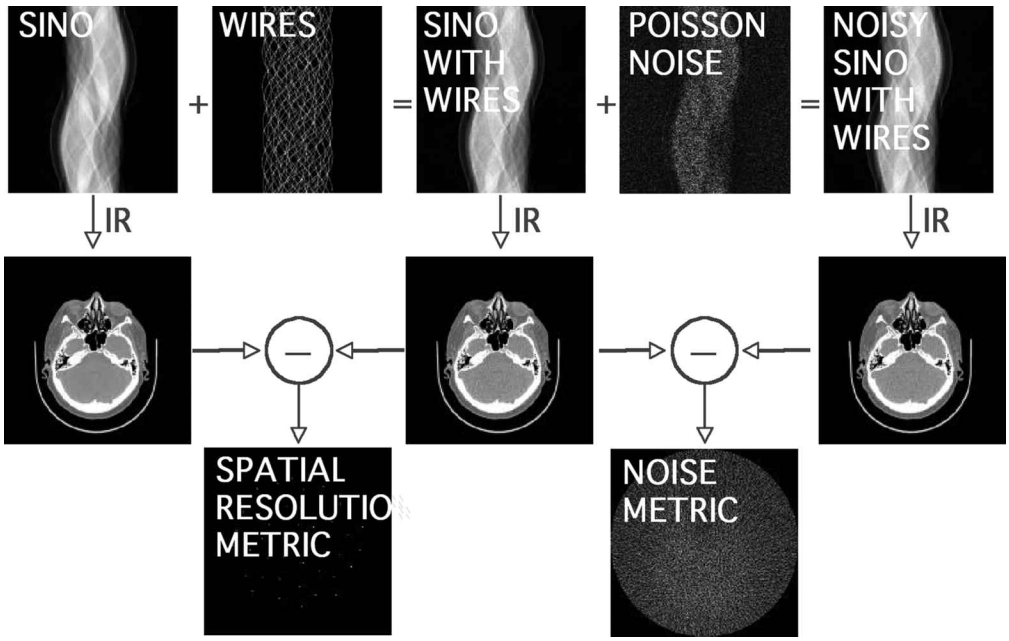

Figure 7. Schedule for assessing spatial resolution and image noise as a function of location and contrast. Artificial noise and impulse responses are added to the original sinogram, reconstructed and subtracted, yielding impulse-only and noise-only images. SEE COLOR PLATE XX.

8 Hardware Implementation Schemes

One of the main challenges in iterative reconstruction is the high computation time. Besides improving the algorithms, one can implement SIR on more powerful hardware architectures. Historically, the fastest reconstruction was achieved using application-specific integrated circuits (ASICs). With the fast development in reconstruction the high initial cost and time to develop a dedicated new ASIC have made this approach undesired. A higher level of flexibility was achieved with field-programmable gate-arrays (FPGAs), but they suffer from relatively low clock speeds. In the last decade general-purpose processors have benefited from a huge increase in clock speed. This in combination with their combination in clusters and multiprocessor architectures, results in an affordable, high-performance, and most flexible solution. Recently, large investments in the gaming industry have resulted in very fast GPUs and multi-core architectures such as IBM's Cell Broadband Engine (CBE) (Figure 8). Researchers have been studying the use of GPUs[117,118] and cell processors[119,120] for several years, but only recently they have become part of the reconstruction engine in commercial scanners.

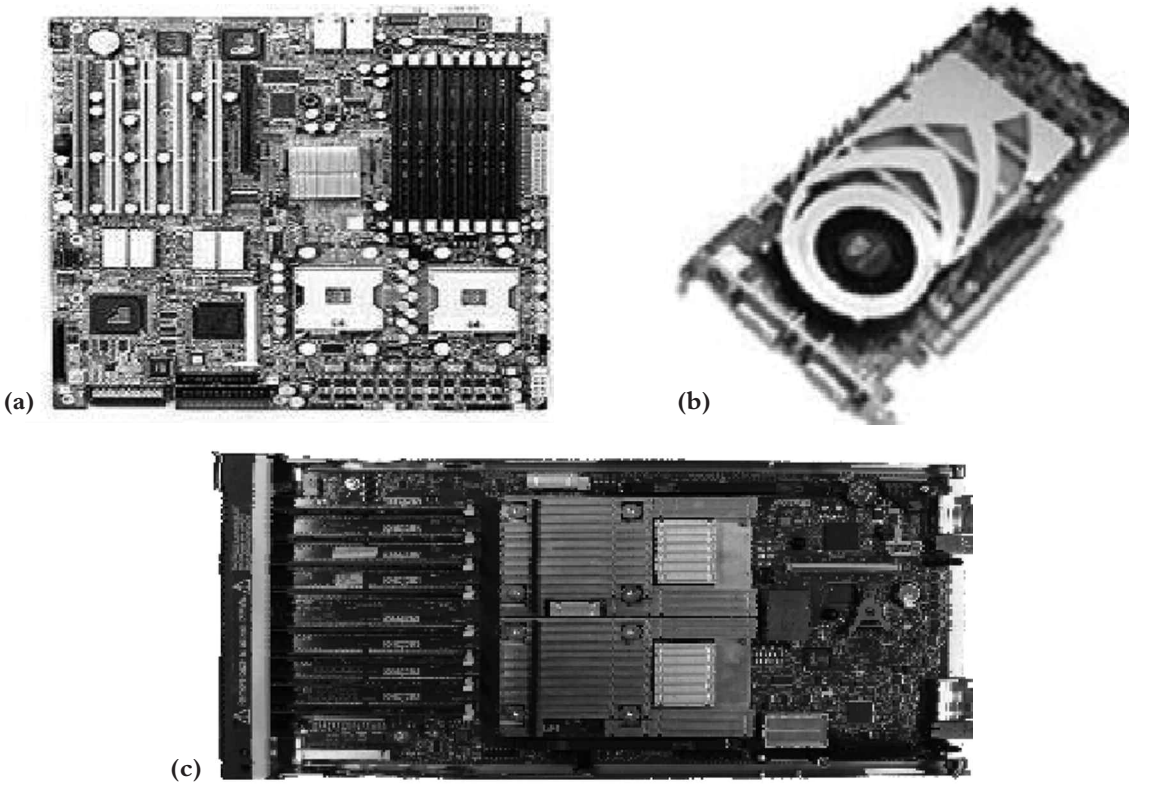

Figure 8. (a) Intel CPU technology, (b) general purpose GPU technology, and (c) Cell Broadband Engine technology. SEE COLOR PLATE XX.

9 Benefits and Applications

The main driver for SIR is undoubtedly its reduced noise (or dose). Figure 9 shows a very low dose patient CT scan reconstructed with FBP and SIR.[20] The SIR images have strongly reduced noise while the spatial resolution is well preserved.

Other potential benefits include its robustness in the case of missing data (metal artifact reduction)[15,26,73,121,122], sparse data (sparse view sampling)[123], and its ability to deal with object motion (cardiac CT).[124–126] Figure 10 shows a CT scan of a Plexiglas™ disk with three amalgam inserts and a number of low-contrast inserts reconstructed with standard FBP and with a maximum *a posteriori* algorithm. The forward model can also include physical effects such as the X-ray spectrum[16,17], the finite beam width[72,73,127], and X-ray scatter. Figure 11 shows a CT scan of a human skull phantom reconstructed with FBP and SIR including a polychromatic spectrum model.

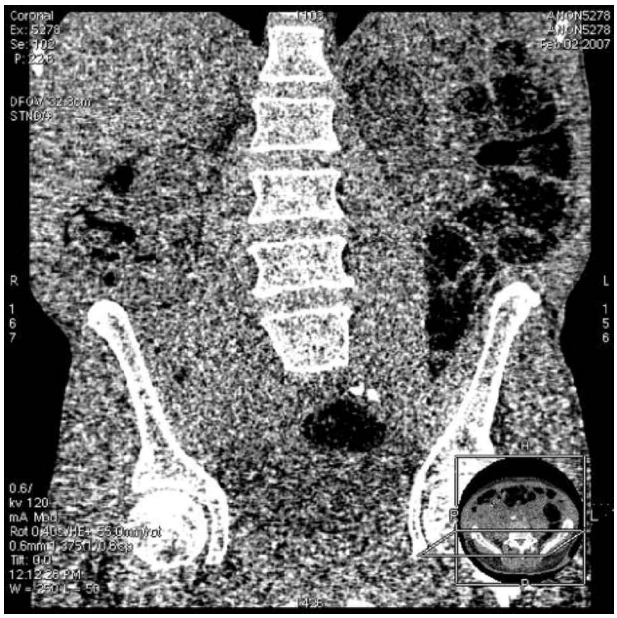

(a)

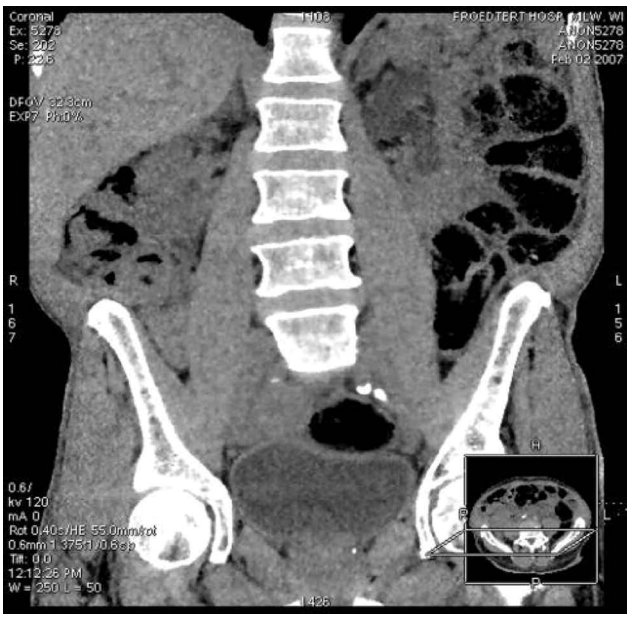

(b)

Figure 9. A very low-dose patient CT scan reconstructed with (a) FBP and (b) SIR.

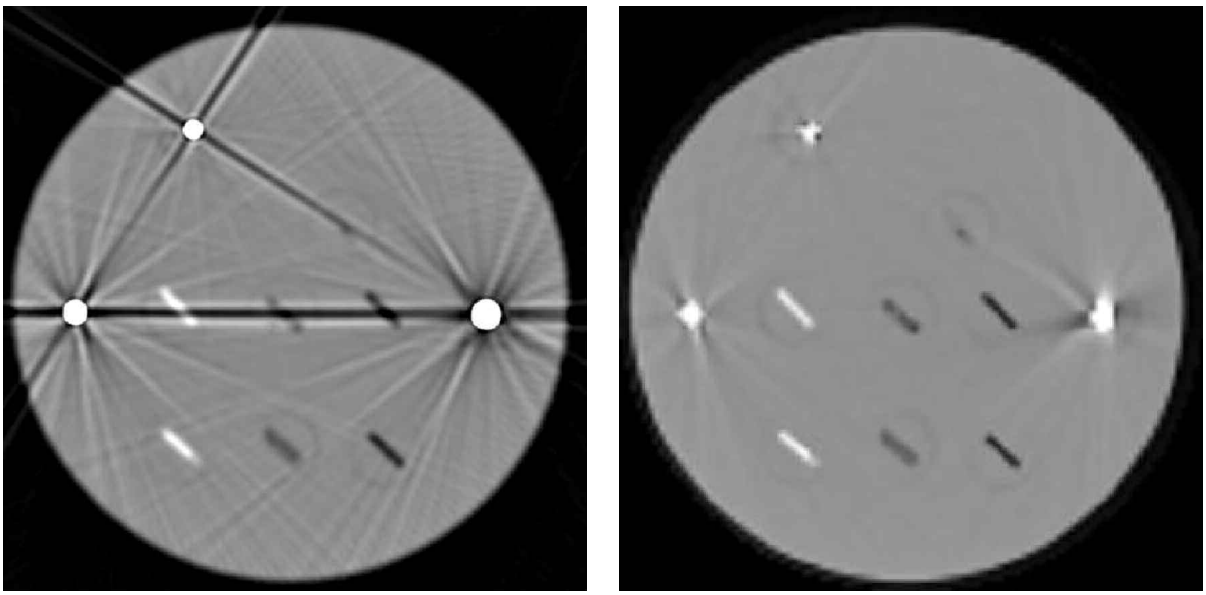

(a) (b)

Figure 10. CT scan of a Plexiglas™ disk with three amalgam inserts and a number of low-contrast inserts reconstructed (a) with standard FBP and (b) with a maximum *a posteriori* algorithm.

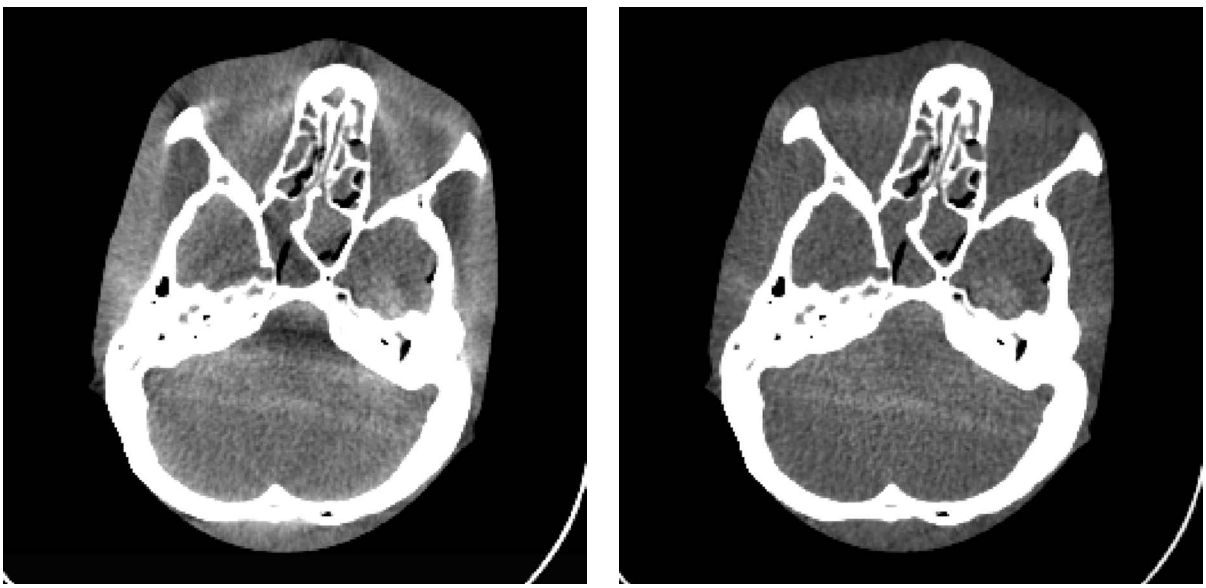

(a) (b)

Figure 11. CT scan of a human skull phantom reconstructed with (a) FBP and (b) SIR with a polychromatic spectrum model.

We have illustrated many potential advantages of SIR relative to FBP. While it would be challenging to suddenly replace FBP, a reconstruction technique with decades of history, by a completely new reconstruction technique like IR, a lot of progress has been made to show the potential clinical impact of SIR, and it is only a matter of time before SIR will become routinely available for clinical application.

References

1. Cormack, A.M. (1963). "Representation of a function by its line integrals, with some radiological applications." *J Appl Phys* 34(9):2722–2727.
2. Cormack, A.M. (1964). "Representation of a function by its line integrals, with some radiological applications. II." *J Appl Phys* 35(10):2908–2913.
3. Ambrose, J., and G. Hounsfield. (1973). "Computerized transverse axial tomography." *Br J Radiol* 46(542): 148–149.
4. Hounsfield, G.N. (1973). "Computerized transverse axial scanning (tomography): Part 1. Description of system." *Br J Radiol* 46:1016–1022.
5. Kaczmarz, S. (1937). "Angenäherte Auflösung von Systemen linearer Gleichungen." *Bull Intl Acad Polon Sci Lettres A*, pp. 335–357. [German]
6. Gordon, R., and G. T. Herman. (1973). "Reconstruction of pictures from their projections." *Comm A C M* 14:759–768.
7. Shepp, L.A., and B.F. Logan. (1974). "The Fourier Reconstruction of a Head Section." *IEEE Trans Nucl Sci* 21:21–43.
8. Bracewell, R.N., and A. C. Riddle. (1967). "Inversion of fan-beam scans in radio astronomy." *Astrophys J* 150:427–434.
9. Ramachandran, G.N., and A.V. Lakshminarayanan. (1971). "Three-dimensional reconstruction from radiographs and electron micrographs." *Proc Natl Acad Sci USA* 68:2236–2240.
10. Rockmore, A.J., and A. Macovski. (1976). "A maximum likelihood approach to emission image reconstruction from projections." *IEEE Trans Nucl Sci* 23(4):1428–1432.
11. Shepp, L.A., and Y. Vardi. (1982). "Maximum likelihood reconstruction for emission tomography." *IEEE Trans Med Imaging* 1(2):113–122.
12. Hudson, H.M., and R.S. Larkin. (1994). "Accelerated image reconstruction using ordered subsets of projection data." *IEEE Trans Med Imaging* 13(4):601–609.
13. Browne, J.A., and T.J. Holmes. (1994). "Developments with maximum-likelihood x-ray computed tomography: initial testing with real data." *Appl Opt* 33(14):3010–3022.
14. Nuyts, J., B. De Man, P. Dupont, M. Defrise, P. Suetens and L. Mortelmans. (1998). "Iterative reconstruction for helical CT: a simulation study." *Phys Med Biol* 43:729–737.
15. De Man, B., J. Nuyts, P. Dupont, G. Marchal, and P. Suetens. (2000). "Reduction of metal streak artifacts in X-ray computed tomography using a transmission maximum *a posteriori* algorithm." *IEEE Trans Nucl Sci* 47(3):977–981.
16. De Man, B., J. Nuyts, P. Dupont, G. Marchal, and P. Suetens. (2001). "IMPACT: Iterative maximum-likelihood polychromatic algorithm for computed tomography." *IEEE Trans Med Imaging* 20(10):999–1008.

17. Elbakri, I.A., and J. A. Fessler. (2002). "Statistical image reconstruction for polyenergetic X-ray computed tomography." *IEEE Trans Med Imaging* 21(2):89–99.
18. Keesing, D.B., J.A. O'Sullivan, D.G. Politte, and B.R. Whiting. (2006). "Parallellization of a fully 3D CT iterative reconstruction algorithm." IEEE International Symposium on Biomedical Imaging (ISBI 2006).
19. Kachelrieß, M., T. Berkus, and W.A. Kalender. (2004). "Quality of statistical reconstruction in medical CT." IEEE Medical Imaging Conference 2003, M10-325.
20. Thibault, J.-B., K. Sauer, C. Bouman, and J. Hsieh. (2007). "A three-dimensional statistical approach to improved image quality for multi-slice helical CT." *Med Phys* 34(11):4526–4544.
21. Ziegler, A., T. Nielsen, and M. Grass. (2008). "Iterative reconstruction of a region of interest for transmission tomography." *Med Phys* 35(4):1317–1327.
22. Herman, G.T. *Image Reconstruction from Projections.* Orlando, FL: Academic, p. 63, 1980.
23. Siddon, R.L. (1985). "Fast calculation of the exact radiological path for a three-dimensional CT array." *Med Phys* 12(2):252–255.
24. Zeng, G., and G. Gullberg. (1993). "A ray-driven backprojector for backprojection filtering and filtered backprojection algorithms." IEEE Nuclear Science Symposium on Medical Imaging Conference, San Francisco, pp. 1199–1201.
25. Joseph, P.M. (1983). "An improved algorithm for reprojecting rays through pixel images." *IEEE Trans Med Imaging* 1(3):192–196.
26. Wang, G., M.W. Vannier, and P.-C. Cheng. (1999). "Iterative X-ray cone-beam tomography for metal artifact reduction and local region reconstruction." *Microsc Microanal* 5(1):58–65.
27. De Man, B., and S. Basu. (2002). "Distance-driven Projection and Backprojection" in IEEE Nuclear Science Symposium and Medical Imaging Conference, Norfolk, Virginia.
28. De Man, B. and S. Basu. (2004). "Distance-driven projection and backprojection: Extension to three dimensions and analysis." *Phys Med Biol* 49:2463–2475.
29. Herman, G.T., and A. Lent. (1976). "Iterative reconstruction algorithms." *Comput Biol Med* 6(4):273–294.
30. Censor,Y. (1983). "Finite series expansion reconstruction methods." *Proc IEEE* 71(3):409–419.
31. Hanson, K.M., and G. W. Wecksung. (1985). "Local basis-function approach to computed tomography." *Appl Opt* 24(23):4028–4039.
32. Lewitt, R. M. and S. Matej. (2003). "Overview of methods for image reconstruction from projections in emission computed tomography." *Proc IEEE* 91(10):1588–1611.
33. Barrett, H.H., and H.C. Gifford. (1994). "Cone-beam tomography with discrete data sets." *Phys Med Biol* 39(3):451–476.
34. Hansen, E. W. (1981). "Theory of circular harmonic image reconstruction." *J Opt Soc Am* 71(3):304–308.
35. Sahiner, B., and A. E. Yagle. (1995). "Region-of-interest tomography using exponential radial sampling." *IEEE Trans Imag Processing* 4(8):1120–1127.
36. Kisilev, P., M. Zibulevsky, and Y. Zeevi. (2001). "Wavelet representation and total variation regularization in emission tomography" in Proceedings of IEEE International Conference on Image Processing 1: 702–705.
37. Rossi, D.J., and A.S. Willsky. (1984). "Reconstruction from projections based on detection and estimation of objects—Parts I & II: Performance analysis and robustness analysis." *IEEE Trans Acoust Speech Signal Processing* 32(4):886–906.

38. Mueller, S.P., M.F. Kijewski, S.C. Moore, and B.L. Holman. (1990). "Maximum-likelihood estimation: A mathematical model for quantitation in nuclear medicine." *J Nucl Med* 31(10):1693–1701.
39. Reyes, M., G. Malandain, P.M. Koulibaly, M.A. Gonzalez-Ballester, and J. Darcourt. (2007). "Model based respiratory motion compensation for emission tomography image reconstruction." *Phys Med Biol* 52(12): 3579–3600.
40. Lewitt, R. M. (1990). "Multidimensional digital image representations using generalized Kaiser-Bessel window functions." *J Opt Soc Am A* 7(10):1834–1846.
41. Minerbo, G. (1979). "MENT: A Maximum entropy algorithm for reconstructing a source from projection data." *Comput Graphics Image Process* 10(1):48–68.
42. Durrani, T.S., and C. E. Goutis. (1980). "Optimisation techniques for digital image reconstruction from their projections." *Proc IEEE Comput Digital Tech, pt. E* 10(1):48–68.
43. Natterer, F. (1980). "Efficient implementation of optimal algorithms in computerized tomography." *Math Methods Appl Sci* 2:545–555.
44. Buonocore, M.H., W.R. Brody, and A. Macovski. (1981). "A natural pixel decomposition for two dimensional image reconstruction." *IEEE Trans Biomed Engr* 28(2):69–78.
45. Hsieh, Y.-L., G.L. Zeng, and G.T. Gullberg. (1998). "Projection space image reconstruction using strip functions to calculate pixels more 'natural' for modeling the geometric response of the SPECT collimator." *IEEE Trans Med Imaging* 17(1):24–44.
46. Delaney, A.H., and Y. Bresler. (1996). "A fast and accurate Fourier algorithm for iterative parallel-beam tomography." *IEEE Trans Imag Process* 5(5):740–753.
47. Horbelt, S., M. Liebling, and M. Unser. (2002). "Discretization of the Radon transform and of its inverse by spline convolutions." *IEEE Trans Med Imaging* 21(4):363–376.
48. Snyder, D.L., and M.I. Miller. (1985). "The use of sieves to stabilize images produced with the EM algorithm for emission tomography." *IEEE Trans Nucl Sci* 32:3864–3872.
49. Kiebel, S.J., R. Goebel, and K.J. Friston. (2000). "Anatomically informed basis functions." *NeuroImage* 11(6):656–667.
50. Hamill, J., and T. Bruckbauer. (2002). "Iterative reconstruction methods for high-throughput PET tomographs." *Phys Med Biol* 47(15):2627–2636.
51. Snyder, D.L. (1984). "Utilizing side information in emission tomography." *IEEE Trans Nucl Sci* 31(1):533–537
52. Carson, R.E., and K. Lange. (1985). "The EM parametric image reconstruction algorithm." *J Am Stat Assoc* 80(389):20–22.
53. Carson, R.E., M.V. Green, and S.M. Larson. (1985). "A maximum likelihood method for calculation of tomographic region-of-interest (ROI) values." (Abstract Book). *J Nucl Med* 26:P20.
54. Carson, R.E. (1986). "A maximum likelihood method for region-of-interest evaluation in emission tomography." *J Comput Assist Tomogr* 10(4):654–663.
55. Formiconi, A.R. (1993). "Least squares algorithm for region-of-interest evaluation in emission tomography." *IEEE Trans Med Imaging* 12(1):90–100.
56. Reutter, B.W., G.T. Gullberg, and R.H. Huesman. (1998). "Kinetic parameter estimation from attenuated SPECT projection measurements." *IEEE Trans Nucl Sci* 45(6):3007–3013.
57. Mazur, E.J., and R. Gordon. (1995). "Interpolative algebraic reconstruction techniques without beam partitioning for computed tomography." *Med Biol Eng Comput* 33(1):82–86.

58. Chiao, P.C. , W.L. Rogers, N.H. Clinthorne, J.A. Fessler, and A.O. Hero. (1994). "Model-based estimation for dynamic cardiac studies using ECT." *IEEE Trans Med Imaging* 13(2):217–226.
59. Hebert, T., R. Leahy, and M. Singh. (1988). "Fast MLE for SPECT using an intermediate polar representation and a stopping criterion." *IEEE Trans Nucl Sci* 35(1):615–619.
60. Kaufman, L. (1987). "Implementing and accelerating the EM algorithm for positron emission tomography." *IEEE Trans Med Imaging* 6(1):37–51.
61. Israel-Jost, V., P. Choquet, S. Salmon, C. Blondet, E. Sonnendrucker, and A. Constantinesco. (2006). "Pinhole SPECT imaging: compact projection/backprojection operator for efficient algebraic reconstruction." *IEEE Trans Med Imaging* 25(2):158–167.
62. Eggermont, P.B. (1983). "Tomographic reconstruction on a logarithmic polar grid." *IEEE Trans Med Imaging* 2(1):40–48.
63. Sitek, A., R.H. Huesman, and G.T. Gullberg. (2006). "Tomographic reconstruction using an adaptive tetrahedral mesh defined by a point cloud." *IEEE Trans Med Imaging* 25(9):1172–1179.
64. Yendiki, A., and J.A. Fessler. (2004). "A comparison of rotation- and blob-based system models for 3D SPECT with depth-dependent detector response." *Phys Med Biol* 49(11):2157–2168.
65. Lewitt, R. M. (1992). "Alternatives to voxels for image representation in iterative reconstruction algorithms." *Phys Med Biol* 37(3):705–716.
66. Matej, S., G.T. Herman, T.K. Narayan, S.S. Furuie, R.M. Lewitt, and P.E. Kinahan. (1994). "Evaluation of task-oriented performance of several fully 3D PET reconstruction algorithms." *Phys Med Biol* 39(3): 355–367.
67. Matej, S., and R.M. Lewitt. (1995). "Efficient 3D grids for image reconstruction using spherically symmetric volume elements." *IEEE Trans Nucl Sci* 42(4):1361–1370.
68. Matej, S., and R.M. Lewitt. (1996). "Practical considerations for 3-D image reconstruction using spherically symmetric volume elements." *IEEE Trans Med Imaging* 15(1):68–78.
69. Carvalho, B.M., and G.T. Herman. (2003). "Helical CT Reconstruction from Wide Cone-Beam Angle Data Using ART" in SIBGRAPI, XVIth Brazilian Symposium on Computer Graphics and Image Processing, pp. 363–70.
70. Chlewicki, W., F. Hermansen, and S. B. Hansen. (2004). "Noise reduction and convergence of Bayesian algorithms with blobs based on the huber function and median root prior." *Phys Med Biol* 49(20):4717–4730.
71. Zbijewski, W., and F.J. Beekman. (2006). "Comparison of methods for suppressing edge and aliasing artefacts in iterative x-ray CT reconstruction." *Phys Med Biol* 51(7):1877–1890.
72. Browne, J A., J.M. Boone, and T.J. Holmes. (1995). "Maximum-likelihood X-ray computed tomography finite-beamwidth considerations." *Appl Opt* 34(23):5199–5209.
73. De Man, B. (2001b). Iterative Reconstruction for Reduction of Metal Artifacts in CT. Ph.D. Thesis. http://perswww.kuleuven.be/~u0015224/.
74. Glover, G.H., and N. J. Pelc. (1980). "Nonlinear partial volume artifacts in X-ray computed tomography." *Med Phys* 7(3):238–248.
75. Joseph, P.M., and R.D. Spital. (1981). "The exponential edge-gradient effect in X-ray computed tomography." *Phys Med Biol* 26(3):473–487.
76. Matej, S., and R. M. Lewitt. (2001). "3D-FRP: direct Fourier reconstruction with Fourier reprojection for fully 3-D PET." *IEEE Trans Nucl Sci* 48(4-2):1378–1385.
77. Matej, S., J.A. Fessler, and I.G. Kazantsev. (2004). "Iterative tomographic image reconstruction using Fourier-based forward and back-projectors." *IEEE Trans Med Imaging* 23(4):401–412.

78. Zhang-O'Connor, Y. and J.A. Fessler. (2006). "Fourier-based forward and back-projectors in iterative fan-beam tomographic image reconstruction." *IEEE Trans Med Imaging* 25(5):582–589.
79. Fessler, J.A. (2004). "Matlab tomography toolbox." Available from http://www.eecs.umich.edu/~fessler.
80. Basu, S., and Y. Bresler. (2002). "O(N3 log N) backprojection algorithm for the 3-D Radon transform." *IEEE Trans Med Imaging* 21(2):76–88.
81. Brokish, J., and Y. Bresler. (2004). "A Hierarchical Algorithm for Fast Backprojection in Helical Conebeam Tomography" in Proceedings of the IEEE International Symposium on Biomedical Imaging, p. 1420.
82. Xu, J., and B. Tsui, (2008). "Electronic noise compensation in iterative x-ray CT reconstruction." *Proc SPIE Med Imaging*, vol. 6913.
83. Hebert, T., and R. Leahy. (1989). "A Bayesian Reconstruction Algorithm for Emission Tomography Using a Markov Random Field Prior" in *SPIE Medical Imaging III: Image Processing* 1092:458–466.
84. Mumcuoglu, E.U., R.M. Leahy, and S.R. Cherry. (1996). "Bayesian reconstruction of PET images: Methodology and performance analysis." *Phys Med Biol* 41(9):1777–1807.
85. Geman, S., and D. E. McClure. (1987). "Statistical methods for tomographic image reconstruction." *Bull Int Stat Inst* 52(4):5–21.
86. Bouman, C.A., and K. Sauer. (1993). "A generalized Gaussian image model for edge-preserving MAP estimation." *IEEE Trans Imag Process* 2(3):296–310.
87. De Man, B. and S. Basu. (2005). "Generalized Geman Prior for Iterative Reconstruction" in 14th International Conference of Medical Physics, Nuremberg, Germany.
88. Mumcuoglu, E.U., R. Leahy, S.R. Cherry, and Z. Zhou. (1994). "Fast gradient-based methods for Bayesian reconstruction of transmission and emission PET images." *IEEE Trans Med Imaging* 13(3):687–701.
89. Qi, J., and R.M. Leahy. (2000). "Resolution and noise properties of MAP reconstruction for fully 3D PET." *IEEE Trans Med Imaging* 19(5):493–506.
91. Fessler, J.A. "Statistical Image Reconstruction Methods for Transmission Tomography" in *Handbook of Medical Imaging. Volume 2. Medical Image Processing and Analysis.* M. Sonka and J.M. Fitzpatrick (eds.). Bellingham, WA: SPIE, pp. 1–70, 2000.
90. Reader, A.J., S. Ally, F. Bakatselos, R. Manavaki, R.J. Walledge, A.P. Jeavons, P.J. Julyan, S. Zhao, D.L. Hastings, and J. Zweit. (2002). "One-pass list-mode EM algorithm for high-resolution 3-D PET image reconstruction into large arrays." *IEEE Trans Nucl Sci* 49(3):693–699.
92. Elbakri, I.A. (2003). Statistical Reconstruction Algorithms for Polyenergetic X-Ray Computed Tomography. Ph.D. Thesis. The University of Michigan, Ann Arbor, Michigan.
93. Srivastava, S., and J.A. Fessler. (2005). "Simplified statistical image reconstruction algorithm for polyenergetic X-ray CT." IEEE Nuclear Science Symposium and Medical Imaging Conference 3:1551–1555.
94. De Man, B. and S. Basu. (2005). "An Efficient Maximum-Likelihood Reconstruction Algorithm for Transmission Tomography and a Generalized Geman Prior." Radiological Society of North America, Chicago, Illinois.
95. Jacobson, M.W., and J.A. Fessler. (2007). "An expanded theoretical treatment of iteration-dependent majorize-minimize algorithms." *IEEE Trans Imag Process* 16(10):2411–2422.
96. Fessler, J.A., and S.D. Booth. (1999). "Conjugate-gradient preconditioning methods for shift-variant PET image reconstruction." *IEEE Trans Imag Process* 8(5):688–699.
97. Sauer, K., and C. Bouman. (1993). "A local update strategy for iterative reconstruction from projections." *IEEE Trans Signal Processing* 41(2):534–548.
98. Fessler, J.A. (1994). "Penalized weighted least-squares image reconstruction for positron emission tomography." *IEEE Trans Med Imaging* 13(2):290–300.

99. Bouman, C.A., and K. Sauer. (1996). "A unified approach to statistical tomography using coordinate descent optimization." *IEEE Trans Imag Process* 5(3):480–492.
100. De Man, B., S. Basu, J.-B. Thibault, J. Hsieh, J.A. Fessler, C. Bouman, and K. Sauer. (2005). "A Study of Different Minimization Approaches for Iterative Reconstruction in X-Ray CT" in IEEE Nuclear Science Symposium and Medical Imaging Conference, Puerto Rico.
101. Yu, Z., J.-B. Thibault, C.A. Bouman, K.D. Sauer, and J. Hsieh. (2007). "Non-homogeneous updates for the iterative coordinate descent algorithm." *Proc SPIE* 6498, Computational Imaging V, page 64981B.
102. Manglos, S.H., G.M. Gagne, A. Krol, F.D. Thomas, and R. Narayanaswamy. (1995). "Transmission maximum-likelihood reconstruction with ordered subsets for cone beam CT." *Phys Med Biol* 40(7):1225–1241.
103. Ahn, S., and J.A. Fessler. (2003). "Globally convergent image reconstruction for emission tomography using relaxed ordered subsets algorithms." *IEEE Trans Med Imaging* 22(5):613–626.
104. Ahn, S., J.A. Fessler, D. Blatt, and A.O. Hero. (2006). "Convergent incremental optimization transfer algorithms: Application to tomography." *IEEE Trans Med Imaging* 25(3):283–296.
105. Fessler, J.A. (1997). "Grouped coordinate descent algorithms for robust edge-preserving image restoration" *Proc SPIE* 3170:184–194.
106. Fessler, J.A., E.P. Ficaro, N.H. Clinthorne, and K. Lange. (1997). "Grouped-coordinate ascent algorithms for penalized-likelihood transmission image reconstruction." *IEEE Trans Med Imaging* 16(2):166–175.
107. Jiang, M., and G. Wang. (2003). "Convergence of the simultaneous algebraic reconstruction technique (SART)." *IEEE Trans Imag Process* 12(8):957–961.
108. Fessler, J. A. and W. L. Rogers. (1996). "Spatial resolution properties of penalized-likelihood image reconstruction methods: Space-invariant tomographs." *IEEE Trans Imag Process* 5(9):1346–1358.
109. Stayman, J.W., and J.A. Fessler. (2000). "Regularization for uniform spatial resolution properties in penalized-likelihood image reconstruction." *IEEE Trans Med Imaging* 19(6):601–615.
110. Stayman, J.W., and J.A. Fessler. (2004). "Compensation for nonuniform resolution using penalized likelihood reconstruction in space-variant imaging systems." *IEEE Trans Med Imaging* 23(3):269–284.
111. Shi, H., and J.A. Fessler. (2005). "Quadratic regularization design for 3D cylindrical PET" in IEEE Nuclear Science Symposium and Medical Imaging Conference 4:2301–2305.
112. Shi, H., and J.A. Fessler. (2006). "Quadratic regularization design for 3D axial CT" in Proceedings of the IEEE Nuclear Science Symposium and Medical Imaging Conference, pp. 2834–2836.
113. Shi, H., and J.A. Fessler. (2008). "Quadratic regularization design for 2D CT." *IEEE Trans Med Imaging*. To appear as TMI-2008-0455.
114. Ahn, S., and R.M. Leahy. (2008). "Analysis of resolution and noise properties of nonquadratically regularized image reconstruction methods for PET." *IEEE Trans Med Imaging* 27(3):413–424.
115. Iatrou, M., B. De Man, K. Khare, and T.M. Benson. (2007). "A 3D Study Comparing Filtered Backprojection, Weighted Least Squares, and Penalized Weighted Least Squares for CT Reconstruction" in IEEE Nuclear Science Symposium and Medical Imaging Conference, Honolulu.
116. De Man, B., M. Iatrou, and S. Basu. (2006). "A Practical Method for Measuring Spatial Resolution in CT and its Application to Iterative Reconstruction." Imaging 2006, Stockholm, Sweden.
117. Mueller, K., and R. Yagel. (2000). "Rapid 3D cone-beam reconstruction with the Algebraic Reconstruction Technique (ART) by using texture mapping hardware." *IEEE Trans Med Imaging* 19(12):1227–1237. (Appeared also in Yearbook of Medical Informatics 2002, Schattauer Verlag).

118. Xu, F., K. Mueller, M. Jones, B. Keszthelyi, J. Sedat, and D. Agard. (2008). "On the Efficiency of Iterative Ordered Subset Reconstruction Algorithms for Acceleration on GPUs" MICCAI (Workshop on High-Performance Medical Image Computing & Computer Aided Intervention), New York.
119. Kachelrieß, M., M. Knaup, and O. Bockenbach. (2007). "Hyperfast parallel-beam and cone-beam backprojection using the cell general purpose hardware." *Med Phys* 34(4):1474–1486.
120. Benson, T.M., W. Dixon, and S. Basu. (2007). "3D Filtered Backprojection for Curved Detector Axial Cone-Beam Data on a PlayStation (R) 3" in Proceedings of the 2007 IEEE Nuclear Science Symposium and Medical Imaging Conference, Honolulu, Hawaii.
121. Wang, G., D.L. Snyder, J.A. O'Sullivan, and M.W. Vannier. (1996). "Iterative deblurring for CT metal artifact reduction." *IEEE Trans Med Imaging* 15(5):657–664.
122. Snyder, D.L., J.A. O'Sullivan, B.R. Whiting, R.J. Murphy, J. Benac, J.A. Cataldo, D.G. Politte, and J.F. Williamson. (2001). "Deblurring Subject to nonnegativity constraints when known functions are present with application to object-constrained computerized tomography." *IEEE Trans Med Imaging* 20(10): 1009–1017.
123. Chen, G.-H., J. Tang, and S. Leng, (2008). "Prior image constrained compressed sensing (PICCS)." *Proc SPIE* 6856:685618-685618-14.
124. De Man, B., P. Edic, and S. Basu. (2003). "Phase-weighted sparse-view iterative reconstruction for cardiac CT." European College of Radiology, Vienna, Austria.
125. De Man, B., P.M. Edic, and S. Basu. (2005). "An Iterative Algorithm for Time-Resolved Reconstruction of a CT Scan of a Beating Heart" in The VIIIth International Conference on Fully 3D Reconstruction in Radiology and Nuclear Medicine, Salt Lake City, Utah.
126. Isola, A.A., A. Ziegler, T. Koehler, W.J. Niessen and M. Grass. (2008). "Motion-compensated iterative cone-beam CT image reconstruction with adapted blobs as basis functions." *Phys Med Biol* 53:6777–6797 .
127. Bowsher, J.E., M.P. Tornai, J. Peter, D.E. Gonzalez Trotter, A. Krol, D.R. Gilland, and R.J. Jaszczak. (2002). "Modeling the axial extension of a transmission line source within iterative reconstruction via multiple transmission sources." *IEEE Trans Med Imaging* 21(3):200–215.